de Haas–van Alphen Effect and Fermi Surface of Ferromagnetic Iron*

David R. Baraff†
Department of Physics, University of Chicago, Chicago, Illinois 60637

(Received 14 February 1973)

An investigation of the de Haas–van Alphen effect in ferromagnetic iron is reported. Evidence has been found for several pieces of the minority-spin surface: the lens pockets along Δ, a central electron surface at Γ, the electron balls along Δ, and the hole octahedron at H. Several majority-spin pieces were also identified: the small and intermediate hole pockets at H, the large hole arm piece at H, and the large electron sheet at Γ. Evidence is also found for orbits that lie partly on the hole octahedron and partly on the hole arm surface. We attribute these orbits to two combined sheets, the hybrid octahedron and the hybrid hole arm piece. These two sheets have mixed spin character which implies that the bands which form these surfaces are spin-hybridized. The mixing of bands of opposite spin is believed to be caused by the spin-orbit interaction which resolves the accidental degeneracy produced at a band crossing. The Fermi surface obtained from this investigation is compared with several recent band-structure calculations.

1. INTRODUCTION

The research described in this paper is an extensive de Haas–van Alphen (dHvA) investigation of iron. It was undertaken in an attempt to resolve some of the contradictions and ambiguities in the current theoretical description of ferromagnetic iron. Although the itinerant nature of the electrons responsible for ferromagnetism in iron is now well established,[1] the basic physical principles upon which to base a band-structure calculation are not. This is evident when a detailed comparison among several recent calculations[2–6] is made. It is difficult to determine what approaches are valid without recourse to the experimental data. Although the Fermi-surface geometry determines the energy-band structure only near the Fermi level, it imposes stringent restrictions which a valid band-structure calculation must meet.[7]

This study utilized a number of experimental techniques developed by Stark[8,9] and co-workers which have been proven effective in a number of metals, particularly in nickel.[7,10] Those used in this study included large-amplitude field modulation, cooling the samples by either a He^3 refrigerator or by a He^3-He^4 dilution refrigerator, complete electromagnetic and acoustic shielding of the experimental apparatus by use of a quiet room, and use of a correlation analysis along with recording of data on magnetic tape for computer processing. As a result of these techniques, the signal-to-noise level in this experiment was high enough to resolve a number of the ambiguities associated with previously published data.[4]

The area data obtained in this experiment were inverted wherever possible to yield the $\vec{k}$ vectors of the Fermi surface.[11–13] Guided by the size, shape, and location of the surface in the Brillouin zone, as determined by the symmetry of the area branches, and by the predictions of theory, a coherent model of the Fermi surface was constructed. In the few cases where the data have not been complete enough to invert directly, a geometric model has been constructed *ad hoc* which yields the areas correctly to better than 1% in the (110) plane. The model Fermi surface which fits all the data is compared with the theoretical predictions.

2. MODEL BAND STRUCTURES AND THE FERMI SURFACE

There have been a number of models proposed for the band structure of ferromagnetic iron. One of the first major calculations was undertaken by Wood[2] using the augmented-plane-wave (APW) technique of Slater. He first obtained a paramagnetic band structure; the calculation took no account of the exchange interaction. To obtain a density-of-states curve simulating the ferromagnetic state, he rigidly split the bands for spin-up electrons from those for spin-down by an amount chosen to yield the accepted magneton number. This number can be determined from measurements of the saturation magnetization and the spectroscopic splitting factor. (The spectroscopic splitting factor describes how much of the magnetization is due to the spin magnetization and how much is due to an orbital contribution. In iron, 5% of the magnetization is due to the orbital moment.)

The Brillouin zone for a body-centered-cubic lattice is shown in Fig. 1. The energy bands derived by Wood are shown in Fig. 2. The spin-up bands are identical with the spin-down bands except for their position relative to the Fermi level. Thus, on Fig. 2 the band structure can be represented by one set of bands with the Fermi levels for the bands of opposite spin separated by an appropriate energy. Wood found the band-splitting energy to be 0.14 Ry.

As Wood himself points out, the assumption that

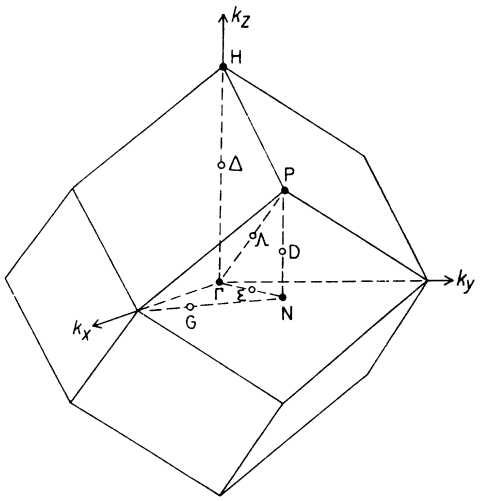

FIG. 1. Brillouin zone for a bcc lattice.

the bands will split rigidly represents an oversimplification of the problem. The exchange splitting even in a simple perturbation treatment is found to be $\vec{k}$ dependent. Another problem with Wood's treatment is that it is not self-consistent in the Hartree-Fock sense, i.e., the calculation has not attempted to adjust the atomic potentials for the charge distribution of the valence electrons.

The calculation by Wakoh and Yamashita[3] (WY) attempted to deal with these objections to the treatment of ferromagnetic iron by Wood. WY included an exchange term in their model Hamiltonian and used an iterative technique to yield a self-consistent treatment of both the majority- and minority-spin carriers. They chose the Green's-function method to calculate the one-electron energy of the points with high symmetry in the Brillouin zone. However, to obtain the potential for the iteration it was necessary for them to use an interpolation scheme to obtain a detailed description of $E(\vec{k})$ throughout the zone. They chose the Slater-Koster scheme.[14] The *d* bands were well represented, although the *s* bands were not. Therefore, in their calculations the number of 4*s*-like electrons was somewhat ambiguous, as was the exact location of the Fermi level. They point out that it would have been desirable to have calculated the energy values at many more points in the Brillouin zone. In spite of these difficulties, the final band structure and resulting Fermi surface is quite similar to that predicted by Wood. The similarities appear in the large pieces of the Fermi surface, which are somewhat insensitive to the exact location of the Fermi level. The most striking difference is that, as expected, the energy difference between opposite spin bands is $\vec{k}$ dependent.

Gold, Hodges, Panousis, and Stone[4] (GHPS) propose a third approach to the description of the band structure of ferromagnetic iron. In their model for the band structure, a pure Slater-Koster interpolation scheme with a tight-binding description of the five 3*d* bands, three 4*p* bands, and one 4*s* band was used. This technique had been used earlier by Cornwell, Hum, and Wong.[15] The tight-binding parameters were chosen to fit the energy values taken from Wood's calculation.

Using this model they were also able to include the effects of spin-orbit coupling. GHPS point out that the simultaneous presence of the ferromagnetic energy plus the spin-orbit term account for some of the most interesting effects seen in the Fermi-surface experiments. (See, for example, the Hodges, Stone, and Gold[16] account of field-induced changes in the geometrical shapes of the X_5 hole pockets in nickel. Also see Stark's description of the mixed-spin orbits in nickel.[10])

The advantages of this choice are threefold[4]: (i) The Fermi surface can be described quickly and accurately. The same amount of information would require the determination of $E(\vec{k})$ at many more points in an APW or Korringa-Kohn-Rostoker (KKR) calculation. (ii) The parameters may be shifted slightly to obtain a better understanding of the effects of band structure on the Fermi surface. (iii) It allows the inclusion of ferromagnetic and spin-orbit interaction terms in a straightforward manner.

It should be pointed out, however, that there are several disadvantages to using such an interpolation scheme: (i) The results of the initial parametrization can be no better than the initial calculation from which the $E(\vec{k})$ values are chosen. (ii) Although the effects of slight shifting of either the Fermi level or the zero energy of a band may be obtained, the physical cause of these shifts is not

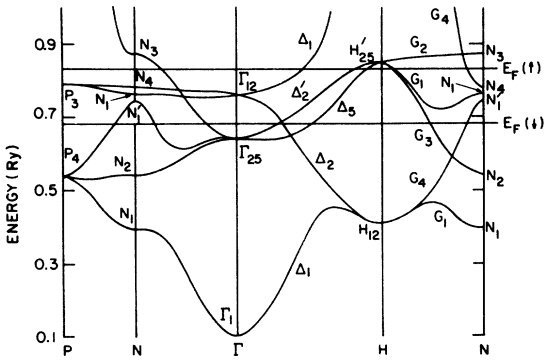

FIG. 2. Energy bands of Wood (Ref. 2) in the principal symmetry directions, with Fermi levels shown for each spin. The labeling of the symmetry points in the Brillouin zone is that which is standard for a bcc crystal. (The figure is taken from GHPS.)

as obvious as in a first-principals calculation. (iii) When the parameters are changed to fit a small amount of experimental data, serious distortions may occur in regions of the Fermi surface for which experimental data were unavailable.

Recently, Maglic and Mueller[5] (MM) have used a Wannier representation of the electron energy in iron. Their interpolation approach uses the energy values calculated by WY. Like GHPS, MM are able to incorporate the effects of the spin-orbit interaction. They too find the hybridization of bands of opposite spin, as suggested by Gold[17] and by Stark.[10]

The mixing of energy bands of opposite spin in a ferromagnetic material is called spin hybridization. In some aspects it may be compared with the s–d hybridization which occurs in transition metals, although the spin mixing leads to several different and important effects worth noting. First, as the band mixing is due to the direction-dependent spin-orbit energy, the energy gap between bands will also be direction dependent. The spin direction depends upon the direction of the internal field, which, in these experiments, lies along the applied field. Thus, as the direction of the applied field is changed, the energy separation between bands of opposite spin will change near the crossing point.

A second point of importance is that in iron the magnitude of the spin-orbit term is quite low. In the free atom the value is about 5 mRy and the value might be expected to be somewhat lower in the solid, where crystal quenching of the orbital angular momentum occurs. Because the gap is small, magnetic breakdown may occur. The treatment of Stark and Falicov[18] may be adopted directly. Using their expression, the breakdown probability P is

$$P = e^{-H_0/B} , \tag{1}$$

where B is the magnetic induction and

$$H_0 \simeq mcE_g^2/\hbar e E_F , \tag{2}$$

where E_g is the energy of the gap across which breakdown occurs, E_F is the Fermi energy, and m is the electron mass. Substituting typical values for iron yields values for the magnetic-breakdown field on the order of 50 kG. This is comparable to the fields in iron. Thus, one expects to observe both normal orbits and breakdown orbits. The normal orbits are the spin-hybridized orbits and the breakdown orbits correspond to what might be expected with no mixing of bands with opposite spin.

The third point to be considered in dealing with hybrid orbits in iron was also treated by Stark and Falicov. In detail, the magnetic-breakdown field is given by the expression

$$H_0 = \pi cE_g^2/4e\hbar v_x v_y , \tag{3}$$

where v_x and v_y are the two components of electron velocity perpendicular to B, v_x being parallel to the Bragg planes and v_y being perpendicular. The magnetic-breakdown probability will depend also on the angle at which the electron approaches the gap.

As a preview of the final results of the experiments, we will discuss the Fermi surface of ferromagnetic iron, which was found to be consistent with our data and moderately consistent with the first-principles band calculations. We shall discuss the surface which might be expected without spin hybridization and point out the effects of spin mixing where it might be expected to occur.

Our experimentally determined Fermi surface is shown in Fig. 3. The different sheets are accorded Roman numerals as follows:

(I) The large spin-up (majority-carriers) electron piece centered at Γ, and commonly referred to as the s-d piece, is found in all models. MM show that in some directions it will be coupled with the spin-down electron balls (VI) along Δ. GHPS imply that magnetic breakdown will cause the unmixed surface to be observed.

(II) The large spin-up hole piece centered at H is found in all models and is called the hole arm piece. Wood and GHPS indicate that these arms, which lie along the line H-N, are pinched off before reaching N. WY show these arms meeting at N, forming a continuous tube structure. MM show these arms mixed by spin hybridization with both the hole ellipsoids at N (VIII) and the hole octahedron at H (V).

(III) The intermediate spin-up hole pocket at H has the interesting feature that magnetic breakdown may occur between it and the hole arm piece. In the absence of spin-orbit coupling the two pieces are degenerate along the line H-P.

(IV) The small spin-up hole pocket has dimen-

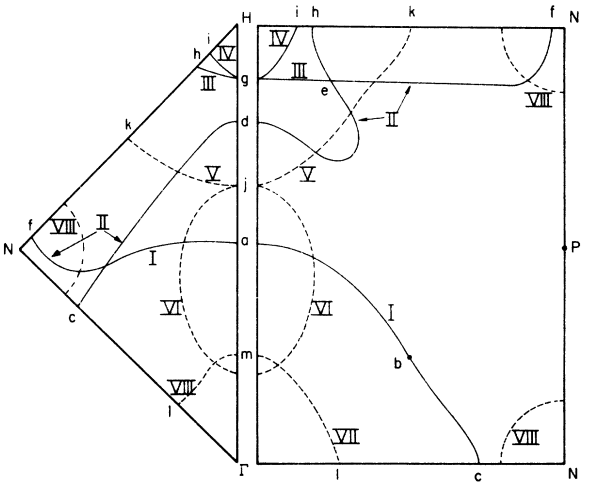

FIG. 3. Experimentally determined Fermi surface. Solid lines are majority-spin pieces and dashed lines are minority-spin pieces.

sions which are quite sensitive to the exact location of the Fermi level with respect to the H'_{25} energy band.

(V) The spin-down hole octahedron is found in all models. MM predict a strong mixing with the hole arm piece.

(VI) The electron balls located along Δ are predicted by all models. The location of these pieces is not only uncertain with respect to the central-electron sheet, but also there is some question about whether or not they hybridize with the *s-d* piece. Also, there is some question as to whether the balls are sufficiently close to the hole octahedron to allow magnetic breakdown to occur. This is important to the magnetoresistance studies in iron, which indicate open orbits in the [100] direction.[19,3]

(VII) The spin-down central-electron sheet is found in all models with minor variations. The main question concerning this piece relates to its exact position with respect to the electron balls (VI) along Δ. In Wood's model there is no overlap, but all others predict the formation of electron lenses along Δ and a neck orbit similar to that observed in tungsten.

(VIII) The spin-down hole ellipsoids are predicted by all models except GHPS and Duff and Das[6] (DD). These two find that the ellipsoids are absent due to a reordering of the energy-band levels near *N*. MM also predict a strong mixing of these ellipsoids with the hole arm piece.

3. EXPERIMENTAL DETAILS

Although the experimental requirements for observing the dHvA effect in paramagnetic materials are well known, we feel that the requirements for a ferromagnet are not well understood, and therefore should be stressed. These techniques have been proven effective in the study of nickel[10] and the present study of iron. A preliminary yet essentially complete description[7] was published as early as 1967, yet apparently the value of these techniques has not been appreciated. In this section we elaborate somewhat on the original details with emphasis given to the reasons for the effectiveness of this experimental configuration.

A. Sample Configuration

Our samples were cut from an iron rod supplied by the American Iron and Steel Institute.[20] This material was specified as having 30-ppm detected metallic impurities and our own mass-spectrographic analysis agreed well with this value. The resistivity ratio of pieces taken at random from this chunk had a maximum value of 400 in an applied field of 800 G. We have no measurements of the Dingle temperature.

Single crystals were located by a light-chemical etching of the surface[21] and were mined from the rod using a spark cutter. The single crystals were carefully aligned using standard back-reflection x-ray methods. Thin disks, 0.1 in. diameter and 0.025 in. thick, were cut from the crystal with the [100] or [110] axis perpendicular to the disk plane. This alignment was made to an accuracy of $\frac{1}{2}°$.

There are a number of reasons for the choice of this geometry rather than some of the other shapes which have been tried. Tsui[7] emphasized that the dHvA effect is only observed if the magnetic induction is homogeneous throughout the sample. The disk, which when electropolished resembles an ellipsoid, enables this requirement to be fulfilled. Secondly, the use of a narrow sample reduces the skin-depth complications that arise due to the modulation field that is used to make the dHvA measurement. If the sample is thicker than the skin depth, the internal volume does not produce any signal. This is equivalent to having poor magnetic coupling with the pickup coil. In effect, a large extra area is required within the pickup coil to surround the sample, and this adds to the noise without materially increasing the signal.

A third advantage of using a thin disk stems from the fact that the demagnetization factor is quite small. In preliminary experiments to determine optimum sample geometry, domain flipping in applied fields as high as 20 kG was observed in a cylinder with a diameter-to-length ratio of one. The amplitude of the voltage generated by these flipping domains was orders of magnitude higher than the dHvA signal. It was concluded that a geometry commensurate with early and *complete* saturation was necessary.

Finally, the requirement of cylindrical symmetry must be met by the sample. The magnetic field is applied in the plane of the samples and is rotated to measure the angular dependence of the signals. Without cylindrical symmetry the demagnetization field will not be constant as a function of angle. This becomes a twofold problem. Firstly, the internal field must be known to determine the dHvA frequencies. If the internal field were to vary, this calibration would have to be made at all angles. Secondly, a fractional change in internal field would add to the noise. The dHvA signal produces an oscillatory internal field of order of 10^{-6} G or less. The average nonoscillatory internal field is about 20 kG. Any fluctuation in this large field can obscure the small signal.

B. Refrigeration Apparatus

The amplitude of the dHvA effect is well known to be dependent upon the temperature in the form

$$A \propto T[\sinh(2\pi^2 kT/\hbar w_c)]^{-1} . \quad (4)$$

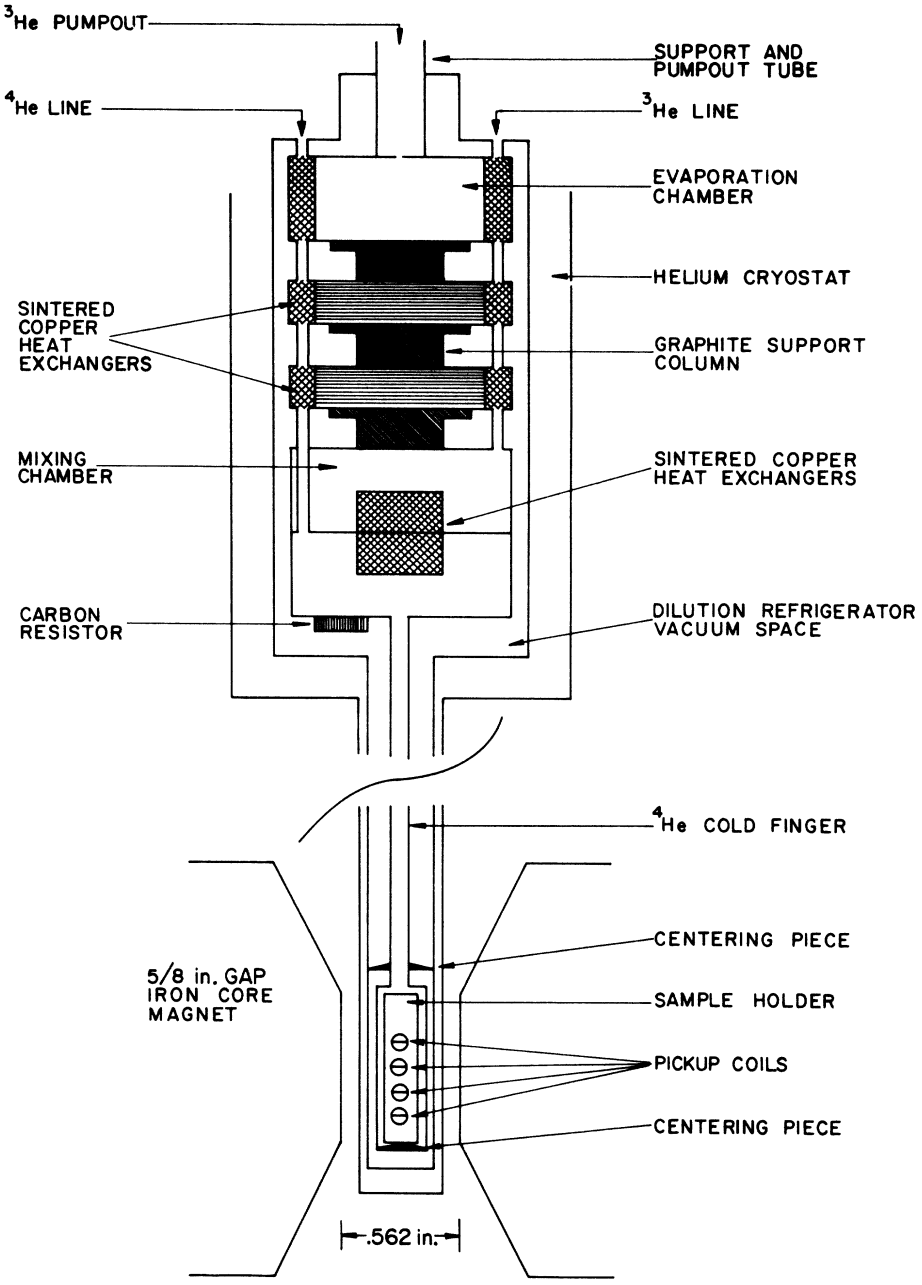

FIG. 4. Schematic diagram of dilution refrigerator in experimental configuration.

It has been pointed out and demonstrated by Stark[22] that, even in samples where the Dingle temperature is on the order of 1 °K, significant gains in signal amplitude are still obtained by going to even lower temperatures if the effective mass is sufficiently large. The flat *d* bands in iron were expected to yield heavy-mass sheets; for example, WY predict a one-electron mass of 2.3 for the hole octahedron. Furthermore, preliminary studies in nickel[7,10] had shown significant increases in the dHvA signal amplitude by going to low temperature.

The He^3 cryostat has been described in detail by Tsui.[7] It was used both for preliminary studies and for separating out some of the signals with larger amplitude. It was capable of cooling the samples to temperatures near 0.3 °K. Temperatures in the region of 0.06 °K were obtained with a dilution refrigerator designed and built by Stark. This device is pictorially represented in Fig. 4. The iron disks were immersed in a bath of He^4 that was in thermal contact with the mixing chamber. The mixing-chamber temperature was monitored by a

Speer carbon resistor.[23] Thermal-time constants at this low temperature were quite long and not accurately known. Unfortunately, we have no mass measurements at present.

C. Detection Apparatus

The low-frequency large-amplitude field-modulation technique has been adequately described in detail.[7–9] It has been noted that the amplitude of the nth-detected harmonic is proportional to $J_n(X)$, where

$$X = 2\pi F \Delta H / B_0^2 \ . \tag{5}$$

Here J_n is a Bessel function, F is the dHvA frequency, ΔH is the modulation field amplitude, and B_0 is the magnetic induction. For a low dHvA frequency in iron ($F \sim 4\times10^6$ G) and typical values of 4×10^4 G for B_0, detecting even on the second Bessel-function peak requires modulation fields of about 200 G. Higher harmonics require higher fields roughly in proportion to the harmonic order detected.

It has been our experience that modulation fields of this size can inductively couple with the superconducting solenoid in such a manner as to create spurious large-amplitude harmonic signals. These unwanted harmonic signals arise in the power supply as it regulates against changes in current. These effects were found to be much reduced in the Varian V-3800 iron-core electromagnet used in this experiment.

Previous experiments had shown that the main source of noise in the detection apparatus was due to vibrations of the sample-pickup coil and wire leads in the magnetic field. A second source of noise was electromagnetic transients from motors, switches, etc. Before the noise level could be significantly reduced, it was necessary to eliminate all vibration. To accomplish this, a completely shielded quiet room was built. The walls were covered inside and out with two layers of metal, 20-gauge silicon steel for magnetic shielding, and galvanized iron for electrical shielding. The two layers were soldered along the edges for good electrical contact. The electromagnetic shielding was better than -120 dB from the low-audio range up to the MHz region.

The acoustic shielding was provided by thick air pockets in the walls as well as by addition of acoustic tile to the inside and outside. The amount of acoustic shielding was about -80 dB. Although the pickup coils were extremely well compensated, the presence of a person breathing or the random occurence of a nitrogen bubble bursting were easily observed on the detection apparatus.

With the quiet room and a special acoustically damped Dewar suspension system (the Dewar support was mounted on a four-layer sandwich of cement blocks and vibration-absorbing rubber mat), the largest source of noise was found to be in the preamplifier. A special preamplifier was built using a low-noise FET supplied by Crystalonics.[24] It had an input impedance of 3 MΩ and an input noise level of 1 nV/Hz$^{1/2}$. Since a number of equivalent preamplifiers of similar quality are now available (Keithley, PAR) we do not include a circuit diagram. (One may be furnished upon request to the author.)

It soon became apparent that in a number of places large-amplitude signals were obscuring low-level dHvA frequencies nearby. Although judicious use of the modulation technique allowed a number of these signals to be separated, it was felt that a magnetic recorder and direct Fourier analysis of the signal would be of use. To this end, we borrowed a system designed and built by Lee. It increased the signal-to-noise level typically by a factor of 30 and was quite useful for disentangling a number of close-lying dHvA area branches.

D. Determination of the Internal Field

The geometry of the samples closely resembles that of a thin lens and the external field is applied in such a way as to be restricted to the equitorial plane of the sample. Above 600 G of applied field, the internal field in the crystal is saturated and essentially lies along the applied field. (See Appendix A.) Therefore, the magnetic induction seen by the electrons is the sum of the applied external field plus the internal field.

The experimental determination of the internal field relied upon the result that the dHvA oscillations are spaced equally in reciprocal B. The positions of eighteen peaks of the dHvA signal were observed and the applied-field reading on the magnet was recorded. To insure that no systematic error was introduced, the points were approached in a random manner except that the dial was rotated in the same direction for the final approach, to eliminate hysteresis effects in the dial. The reproducibility of these peak positions was better than 5 G. Later, an NMR probe replaced the iron sample in the magnetic field and the field values were accurately measured.

The internal field can be found quite directly by fitting the peak number (starting with an arbitrary integer) and the reciprocal of the total field to a straight line. The dHvA frequency and the internal field are treated as variable parameters and the least-squares fit was done by computer. In this way, the internal field could be determined to an accuracy of $\frac{1}{2}\%$.

The internal field is used directly in determining the dHvA frequencies and we believe that it supplies the most significant cause of error in the experiment. Over a small field range ΔH, the dHvA

frequency is given by the formula

$$F = nH^2/\Delta H\ , \tag{6a}$$

where n is the number of complete oscillations and H is the magnetic field. The error in F due to a small error in H is found by differentiating Eq. (6a) as follows:

$$dF = 2nH\delta/\Delta H\ , \tag{6b}$$

where δ is the small error in H. Thus, the relative error in F due to a small error in H is found by dividing Eq. (6b) by Eq. (6a):

$$dF/F = 2\delta/H\ . \tag{6c}$$

The internal field was 20 kG and the total field was typically 40–50 kG. Thus, an error of $\frac{1}{2}\%$ in the internal field yielded an error in the total field of about $\frac{1}{4}\%$. Using Eq. (6c), the error in the determination of the dHvA frequency was $\frac{1}{2}\%$.

The internal field was measured only in the (110) sample. To determine the internal field in the (100) sample the frequencies on the [001] axis which were observed in both samples were compared, and the calibration in the (100) sample was taken from this comparison.

The other main source of error in this experiment was the determination of the end points for field-sweep data. Normally, this error was reduced to a minimum by the bootstrap technique of using one frequency to calibrate another. In this method a well-known frequency is used to determine another. This allows a calibration accuracy of better than $\frac{1}{2}\%$. Thus, as an upper estimate of the errors, the experimental frequencies are determined to within 1% absolute accuracy.

4. RESULTS AND DISCUSSIONS

Since bcc iron has high symmetry, the data were taken only with the applied field in the (100) and (110) planes. The measured dHvA frequencies have been converted to extremal areas on the Fermi surface by the Onsager relation[25]

$$A = 2\pi eF/ch\ . \tag{7}$$

[The area in atomic units (a.u.) equals $2.673 \times 10^{-9}F$; F is given in G.] For convenience in Fig. 5, the ordinate can be read either as an extremal area in a.u. or as a frequency in G. The abscissa is the angular distance in degrees from the [001] axis in either the (100) or (110) plane. The frequency branches are labeled with Greek letters chosen arbitrarily where no correspondence with previously named branches could be found.

It can be noted that the data in the (110) plane are somewhat more complete than those in the (100) plane. This is not an intrinsic feature of iron. The 90° symmetry plane is more complete with data because the signal-to-noise level was higher when

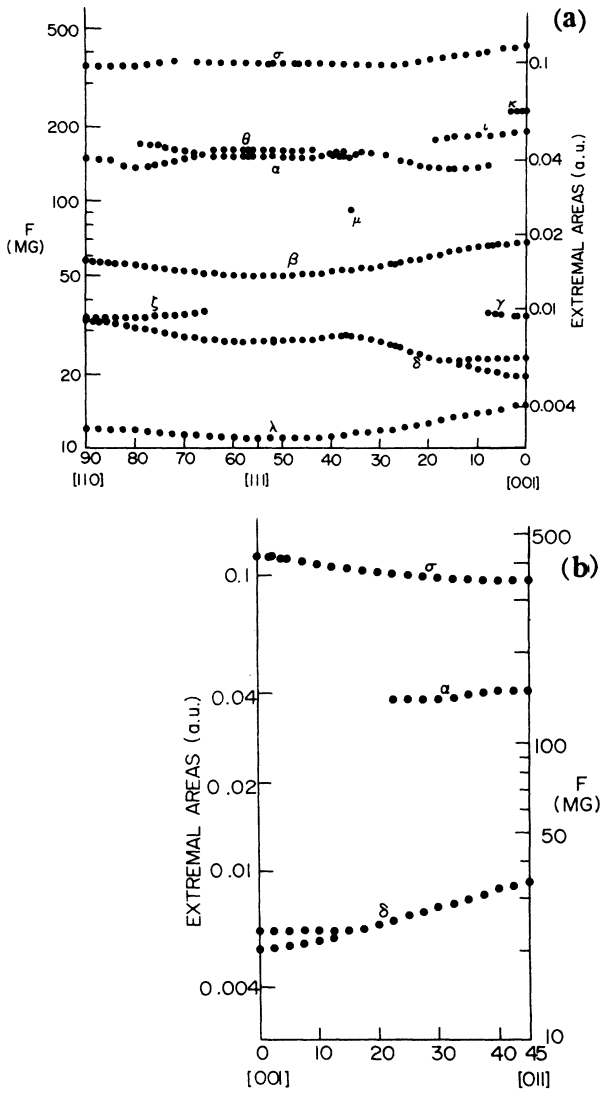

FIG. 5. (a) dHvA spectrum in the (110) plane. (b) dHvA spectrum in the (100) plane. The angles are in degrees.

that sample was studied. The (110) sample was slightly thicker, which resulted in better coupling with the pickup coils and probably also resulted in a greater homogeneity of field within. Also, the experimental run with the (110) sample obtained lower temperatures than that with the (100) sample. It has been noted previously that the low temperature enhances the signals from orbits with large effective mass. Finally, neither the low-noise preamplifier nor the digital-recording apparatus were used in the first run. Thus, signals which were clearly present on the [001] axis of the (110) sample were not observed on the [001] axis of the (100) sample.

The lowest frequencies observed were well de-

scribed previously by GHPS and for that reason we have not reproduced them in the main frequency diagram, Fig. 5. Briefly, there are two sets of frequencies not included. One set is attributed to an electron lens along Δ, the other single frequency was attributed to a neck between the two pieces which join to form the lens. The symmetry considerations locate these two orbits quite unambiguously. The GHPS arguments are bolstered by our observations of orbits that can be assigned to the larger pieces, which intersect forming the neck and lens.

The frequency branch β is attributed to the central electron surface (VII) located at Γ. Although GHPS were able to observe this branch only near the [111] direction, we have followed it throughout the (110) plane. The amplitude of the signal falls as the magnetic field approaches either of the major axes. Near the major axes the orbit is believed to be a magnetic breakdown orbit. As suggested by GHPS, the spin-orbit gap may be reduced for this field orientation, which increases the probability that an electron will tunnel. The tunneling probability is less than unity and thus the signal amplitude is smaller near the axes.

The branch labeled γ is believed to arise from an orbit around the electron balls. This branch extends only 8° from the [001] axis before cutting off abruptly. This sudden loss of amplitude is believed to be caused by the intersection of this orbit with the *s-d* piece. With complete hybridization, i.e., a large enough gap to prevent magnetic breakdown, it ought to be possible to continue following the orbit; however, with some breakdown the amplitude would be diminished. As this branch is only about a factor of 3 above the noise level, the exact reduction in signal level is not known. It is greater than a factor of 3.

An interesting comparison can be drawn between these pieces of the Fermi surface of iron and the corresponding Fermi surface in tungsten.[26,27] In tungsten the spin-orbit effect is strong enough to suppress the lens below the Fermi surface. Also, the neck frequency in tungsten reveals a smooth rounded neck that contrasts quite strongly with the frequency from the neck in iron, which drops in amplitude quite rapidly. Furthermore, in tungsten the surface is sufficiently smoothed to allow observation of orbits around both the central-electron piece and the balls. Rather than distinct pieces, as is found in iron, the central-electron piece and balls form a single piece, called the "Jack" for its resemblance to the toy. The large spin-orbit gap makes magnetic breakdown very improbable. This is quite different from iron where *no* orbits around both pieces are found.

As touched upon earlier, the differences between these pieces in iron and tungsten is largely explained by the different magnitude of the spin-orbit energies in the two materials. The spin-orbit energy in tungsten is estimated to be about 30 mRy, whereas estimates for iron are lower typically by a factor of 10. MM suggest a value of 5 mRy; WY suggest a value of 0.8 mRy; and GHPS find an intermediate value of 1.5 mRy. It is probably an oversimplification, in view of earlier discussion, to believe that a single value for the spin-orbit interaction will apply for all cases, as the different bands undoubtedly couple with different strengths.

The branch labeled λ is found to be continuous in the (110) plane. GHPS found it near [111]; however, they apparently were unable to discriminate it from the third harmonic of the neck frequency in the [001] direction and the third harmonic of the lens in the [110] direction. Using the rotation-diagram technique, we have followed this frequency throughout the (110) plane and find it continuous. The frequency determination by the rotation method is in good agreement with the field-sweep data. As a double check, we determined that the second harmonic of this branch existed. It was easily followed in the (110) plane everywhere except for a 10° interval, where it crosses the δ branch (which has an unusually large amplitude that obscures the λ signal.) The λ branch is the orbit around the small spin-up hole pocket at H (IV).

The next branch we discuss is labeled δ. GHPS found this branch near [111] and observed the separate sections of it in the [001] direction. Unfortunately, they were not able to observe the continuity of these branches. Thus they assigned the branch near [111] to the intermediate hole pocket at H and the upper branch at [001] to the electron balls along Δ. (For completeness of description, we also note that there is a 2% splitting of the frequency branch δ in the [111] direction. The higher frequency is a noncentral extremal.)

Figure 6(a) shows a perspective view of the intermediate hole pocket. It can be seen that as the magnetic field is rotated from the [001] direction to the [111] direction, the orbit must pass over the sharp corner when the magnetic field is along the [112] direction. The amplitude within several degrees of the [112] direction is found to drop, and at the axis it is reduced from what it was by a factor of 10, 4° to either side. This indicates both of the geometric effects in reducing the signal amplitude and also suggests magnetic breakdown to the hybrid octahedron. Thus the intermediate hole pocket (III) is the correct assignment of the δ branch.

Magnetic breakdown between the intermediate spin-up hole pocket and the hybrid octahedron is observed quite dramatically through the appearance of the frequency point μ. Figure 6(b) shows a cross section through H perpendicular to the [112] axis. For clarity, only the two pieces of surface involved are shown. One frequency observed in the [112] di-

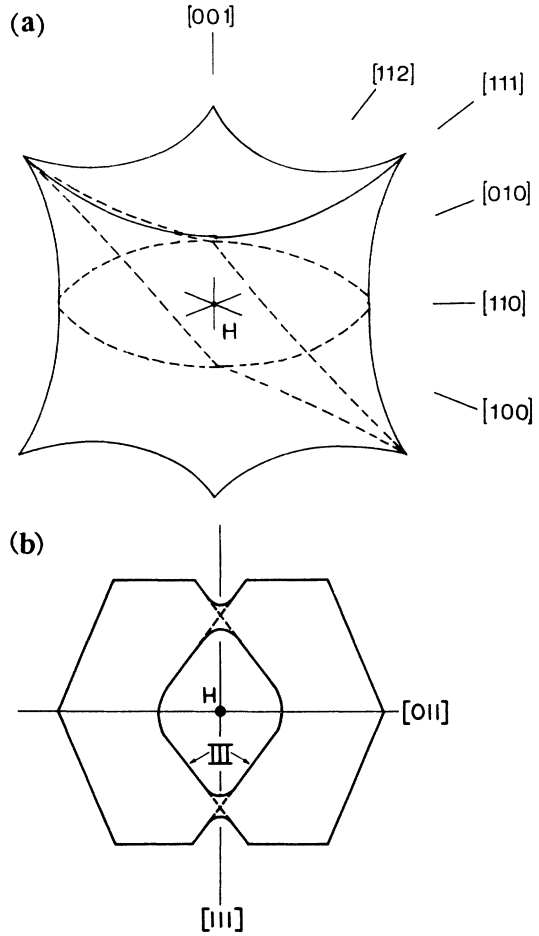

FIG. 6. (a) Perspective view of the intermediate hole pocket at H. Central orbits in the (001) and (112) planes are shown as dashed lines. (b) Central cross section through H in the $(11\bar{2})$ plane, showing the orbits around the hybrid octahedron and the intermediate hole pocket. The dashed lines describe the magnetic breakdown path of the electron, which encircles an area equal the $\frac{1}{2}(A+B)$, where A is the area of the intermediate hole pocket and B is the area of the hybrid octahedron orbit.

rection is on the intermediate hole pocket (III in Fig. 3); another is the orbit around the hybrid octahedron. A third frequency labeled μ in Fig. 5 is observed only within $\frac{1}{2}°$ from the [112] axis. This frequency has a value equal to the sum of one-half that of the α branch at that point and one-half that of the δ branch at that point. Thus, the area encircled by the orbit is one-half the area of the hole pocket and one-half the area of the hybrid octahedron. To complete this orbit the electron must undergo magnetic breakdown twice per orbit. Although many effects may give rise to harmonic terms, we know of no other way to generate terms made from simple fractions of areas than that of coupled orbits.

On most of the branches previously described the data were complete enough to allow the use of the inversion scheme to fit the experimental areas to a geometric shape. Although the data for the hybrid octahedron is quite complete, the same technique was not employed for two reasons. First, crucial values for the central areas were not observed near the fourfold and twofold symmetry axes, although a noncentral extremal is observed in the [110] direction. Second, a combination of sheets into a hybrid surface is expected to create a surface with sharp corners not well suited to expansion by an interpolation scheme using only twelve Kubic harmonics. Therefore, an approach suggested by Stark and Auluck was tried.

A model was constructed of the spin-up hole arm piece and the spin-down hole octahedron following the predictions of the band structure. Each piece was expanded in Kubic harmonics. The areas of the combination piece were calculated by computer and compared with the experimental data. Small changes were introduced into the geometry of the model and a very satisfactory fit was obtained. Figure 7 shows a fit of the model calculation with the experimental data in the (110) plane. No single point from the calculation is in greater error than 1% and, for most, the agreement is better. Although small perturbations of the model might produce as good a fit to the area data, we feel that the general topology must be approximated to a high degree.

The branch which is due to the hybrid octahedron is labeled α. In Fig. 7 it is shown together with the points from the calculation. In the (100) plane it was followed for 22° from the [011] axis before it was abruptly lost. In the (011) plane it was followed from the [011] axis to within 10° of the [001] axis. The noncentral extremal joins the central orbit 12° from the [011] axis in the (011) plane. Also,

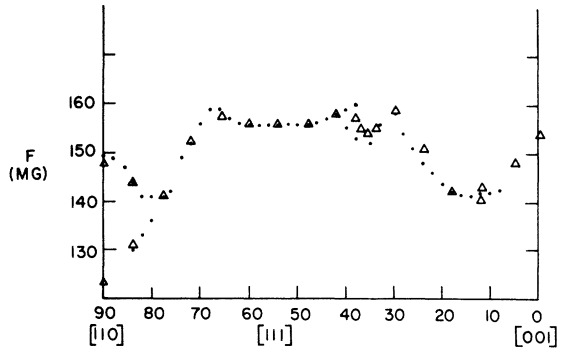

FIG. 7. dHvA spectrum of the α branch, shown in enlarged detail. Solid dots are the experimental frequencies and triangles are the calculated extremal areas of the hybrid octahedron.

there is a noncentral extremal which is less than 1% larger than the central orbit, which appears 11° from the [001] axis in the (011) plane. Both these observations are reproduced by the model.

The hybrid octahedron model is reproduced in Fig. 8(a). The noncentral extremal near the [011] axis is shown as a line with long and short dashes. The orbit which is observed in the [211] direction is shown as an evenly dashed line. The [211] orbit dips into the funnel-shaped indentations which are in the [111] directions. The indentations on the octahedron are caused by its intersection with the hole arm piece.

The hybrid hole arm piece is shown in Figure 8(b). It strongly resembles the hole arm piece except that small caps of the octahedron appear in the [100] directions and a small piece from the flat face of the octahedron is also hybridized with it. Two noncentral orbits from this piece have been observed. One is a noncentral extremal minimum orbit. In Fig. 5 this frequency branch is labeled θ. The θ branch was not observed at 0.3 °K, although at 60 m °K its amplitude was close to half that of the α branch. This indicates that the mass of the θ branch is larger by about a factor of 2 than the α branch. (This figure is based on the mass of 1.7 for the α branch.[4])

The branch labeled κ is observed only within 2° of the [001] axis, and the frequency variation in this range of observation was less than 1%. Its amplitude was lower than that of the σ branch on the [001] axis. This is somewhat surprising, as the area of the κ branch is about one-half that of the larger frequency. This indicates either a large mass or high rate of scatter for this orbit. We believe it is due to the noncentral maximum on the hybrid hole arm piece.

The branch labeled ι in Fig. 5 is believed to be the magnetic breakdown orbit on the hole octahedron. It has been pointed out previously that directional effects may play a large role in determining what aspects of the Fermi surface in iron may be observed. The amplitude of the hybrid hole arm piece is unobservably small near the [001] axis. This reduction in signal amplitude could be caused by magnetic breakdown, and thus one might expect to observe the breakdown orbit. This orbit would be the unhybridized orbit around the octahedron, which we believe is observed as the ι branch.

The branch labeled ζ in Fig. 5 was observed to extend 26° from the [110] axis in the (110) plane before undergoing a sharp reduction in amplitude. This reduction in amplitude is similar to that suffered by the γ branch. There is an orbit around the ellipsoids at N which ought to be observed and the ζ branch has its most likely assignment to this orbit. As can be seen in Fig. 3, the orbit around the hole ellipsoids would extend about 30° from the [110] axis before intersecting with the hole arm piece.

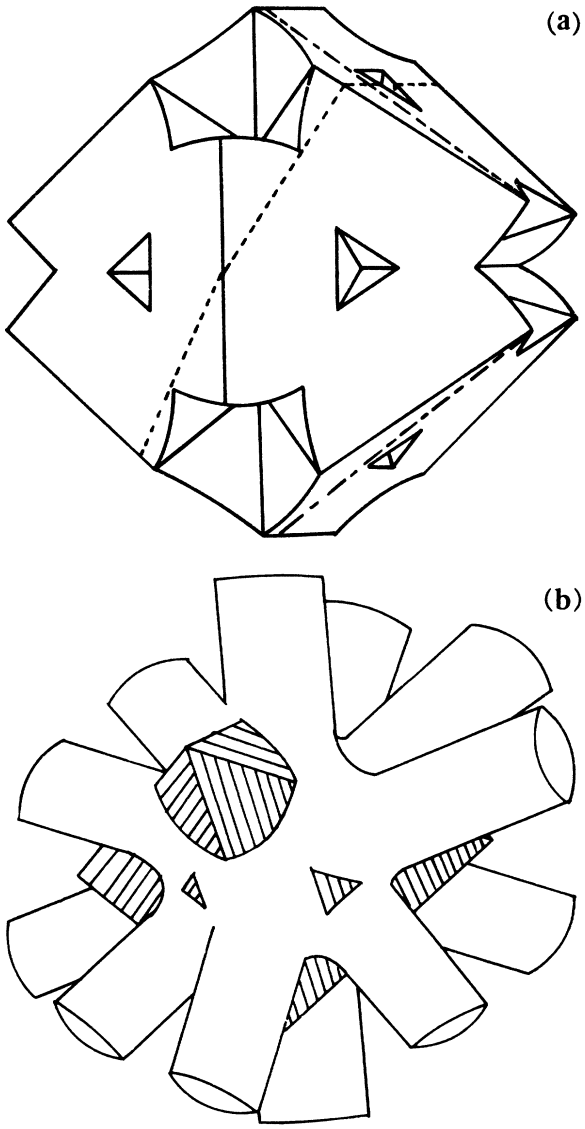

FIG. 8. Hybrid octahedron. The noncentral extremal observed in the (110) plane is shown as an unevenly dashed line. Also, the central orbit in the (211) plane, which breaks down to the intermediate hole pocket is shown as an evenly dashed line. (b) Hybrid hole arm piece.

The final branch we discuss is labeled σ, and is most certainly due to the s-d piece. This branch was followed in both symmetry planes and is continuous everywhere. In the [110] direction it was observed at temperatures as high as 0.4 °K because of an extremely favorable geometry. Two frequencies are present at this axis and join 6° away in the (110) plane. It can be seen in Fig. 5 that near the [001] axis the value of $dF/d\theta$ is quite large. This results in a reduction of amplitude in this region.

TABLE I. Principal Fermi-surface dimensions in units of $2\pi/a$. The point notation is from Fig. 3. Our values are compared with the synthesized values GHPS.

Identification	Experiment	GHPS
Γ-a	0.514	0.51
Γ-b	0.432	0.42
Γ-c	0.495	0.47
Γ-1	0.189	0.19
Γ-m	0.242	
H-e	0.187	0.23
H-g	0.110	0.11
H-h	0.126	0.13
H-i	0.089	0.09

(If a crystal has small subgrain boundaries resulting in a number of small crystals with slightly different alignment, the dHvA signal is reduced due to the phase cancelling of the signal.) However, at the axis, and within the last degree, $dF/d\theta$ is zero and the amplitude ought to increase. It does not. At the [001] axis the signal is at its smallest value. The most likely explanation of this effect seems to be that which GHPS advanced when they failed to detect any signal in this region. Magnetic breakdown can occur between the s-d piece and the hole arm piece. In Fig. 3 this point of tangency is seen in the (100) cross section.

The experimentally observed frequencies were inverted to yield the $\vec{k}$ vectors of the Fermi surface. This inversion was based on Mueller's interpolation scheme[11] using the Kubic harmonics, as derived by Falicov and Lee,[13] and a least-squares computer program written by Stark and Auluck. Table I lists the $\vec{k}$ vectors found in this experiment and compares them with values taken from the semiempirical model of GHPS. The agreement is quite good. The model of GHPS which yielded these $\vec{k}$ vectors apparently used the shapes predicted by their band structure and scaled them to fit the data which was available.

Table II lists some of the measured experimental dHvA frequencies and compares them with some of the theoretical predictions. As is to be expected, the agreement is somewhat better on the larger pieces, where the exact energy of the Fermi level is not as critical for determining the area.

5. CONCLUSION

This dHvA study has been complete enough to determine the $\vec{k}$ vectors of all non-spin-hybridized pieces of the Fermi surface using a direct inversion technique. This process has given some measure of confidence in the general predictions of the band-structure calculations. Using the predictions of these calculations we have generated some spin-hybridized surfaces which fit the remaining data.

We feel, however, that the story is far from complete, either experimentally or theoretically. Several challenging experimental problems remain. At this time, the data on electon masses for the different sheets is quite incomplete. Also, it would be useful to make a more detailed study, which is at present technically quite feasible, of the hybrid orbits. A careful amplitude study would yield more accurate data on the magnetic-breakdown probability which would allow an accurate determination of the spin-orbit energy. Theoretically, there still exists the problem of completing a first-principles calculation to high enough accuracy to agree completely with these experimental results.

ACKNOWLEDGMENTS

I wish to sincerely thank Professor Royal W. Stark for suggesting this problem and for advice and encouragement along the way. I wish also to acknowledge the help of a number of other persons for the contributions they made; Professor M. J. G. Lee for providing the digital recording system; Dr. A. Gaertner for assistance in operating the cryogenic system; Dr. S. Auluck for programming assistance; and C. Friedberg, Dr. F. Richards, and R. Reifenberger for helpful discussions.

APPENDIX A: MAGNETIC ANISOTROPY AND DIRECTION OF THE INTERNAL FIELD

It is well known that the magnetic anisotropy energy in iron can be expressed in the form

$$U_K = K(\alpha_1^2\alpha_2^2 + \alpha_2^2\alpha_3^2 + \alpha_3^2\alpha_1^2) + K_2(\alpha_1^2\alpha_2^2\alpha_3^3)\ ,$$

where U_K is the anisotropy energy, α_1, α_2, and α_3 are the direction cosines with respect to the cube

TABLE II. Experimental dHvA frequencies from four models compared with experimental data. The models A and B are taken from GHPS. The values for Wood's model are also taken from GHPS who calculated the Fermi surface yielded by Wood's energy bands.

Surface Fig. 2	Field direction	Experiment ±1%	WY	Wood	A	B
I	[001]	436	398		436	
	[111]	370		380	372	372
	[110]	349	345	346	358	412
III	[001]	20.6	5.3	10.8	17.6	17.6
	[111]	27.0		13.8	21.9	21.9
	[110]	33.4		21	27	27
IV	[001]	15.0	4.3	9.7	15.7	15.7
	[111]	11.4		8.1	12.4	12.4
	[110]	12.3	3.8	9	15	15
V	[001]	198	226	204	219	219
	[111]	157		133	145	145
VII	[001]	71.0		89	63	
	[111]	52.2		61	49	
	[110]	58.2		74	54	

TABLE III. Kubic harmonic expansion coefficients from experimental data.

Surface	rms error	Coefficients (in order) yield frequencies					
I	0.3%	3.7445	0.2573	0.1140	0.0205	0.0619	0.0423
(10^8 G)		0.0090	0.0366	0.0055	0.0065	0.0396	
III	0.5%	2.7406	−0.5060	−0.1886	0.0114	0.0558	−0.1000
(10^7 G)		0.0672	−0.0345	0.0015	0.0233	−0.0016	
IV	0.6%	1.2416	0.1721	0.0026	0.0560	0.0068	
(10^7 G)							
VII	0.3%	5.8550	0.9595	−0.0266	0.2711	0.0266	
(10^7 G)							

edges, and K_1 and K_2 are the anisotropy coefficients. If an external field H is applied at an angle θ with respect to the direction of the internal field I, the additional energy stored will be $-HI\cos\theta$. To find the angle θ, the derivative of the total energy must be zero. Typical values for K_1 and K_2 are 5×10^5 and 1×10^5 erg/cm^3, respectively. At field strengths of 30 kG, the value for the energy density in the stored field is 3×10^7 erg/cm^3. For small angles, $\sin\theta$—the derivative of $\cos\theta$—may be approximated by θ, and it is seen that until $\theta\simeq0.01$ the magnetic anisotropy may be ignored and that the internal field lies along the applied field to better than $\frac{1}{2}°$.

APPENDIX B: KUBIC HARMONIC EXPANSION COEFFICIENTS FROM THE EXPERIMENTAL DATA

The Kubic harmonic coefficients taken from the experimental data are listed in Table III. The coefficients are listed in the order given in Ref. 13, except that the coefficient for ${}_1K_2$, which is zero, is not listed. These coefficients reproduce the experimental frequencies to the accuracies given below for each different branch.

Before listing the coefficients we feel an additional note of explanation is needed. It has been our experience that although a Kubic harmonic expansion may fit a set of area data very well, there is no simple way to predict the maximum error in the $\vec{k}$ vectors yielded by the interpolation scheme. A set of test areas was generated by computer. These areas were in the (110) or (100) plane, and, following Ref. 12, only the first eleven harmonics were used. As these areas were computer generated, an almost perfect fit, limited only by computer roundoff errors, was possible; however, to better simulate a realistic situation, the program was terminated when the rms error was 0.04%. The maximum single error in area was 0.14%. One might naively assume that the largest error in radius would be of the order of 0.07%; however, the largest radius error was 2%, which is almost thirty times as large as one might expect from a "perfect" inversion.

As appallingly large as this error is, there is an important factor which mitigates the problem. If one considers the Fourier expansion of a square wave using only several harmonic terms, one notes that the value of the series-expansion term fluctuates about the value of the square wave. If one were to draw a line through the central values, the error in that line would probably be much less for all points than the maximum deviation of the Fourier-series point to the square wave. Thus, we believe the $\vec{k}$ vectors of Fig. 3 to be much better than the worst possible error given in the previous example.

---

*Submitted in partial fulfillment of the requirements for Ph.D. in physics at the University of Chicago. This work was supported in part by the Advanced Research Projects Agency and by the National Science Foundation.

†Present address: Department of Physics, University of Toronto, Toronto, Ontario.

[1]C. Herring, in *Magnetism*, edited by G. T. Rado and H. Suhl (Academic, New York, 1967), Vol. 4, Chap. 6.
[2]J. H. Wood, Phys. Rev. **126**, 517 (1962).
[3]S. Wakoh and J. Yamashita, J. Phys. Soc. Jap. **21**, 1712 (1962).
[4]A. V. Gold, L. Hodges, P. T. Panousis, and D. R. Stone, Int. J. Magn. **2**, 357 (1971).
[5]R. Maglic and F. M. Mueller, Int. J. Magn. **1**, 289 (1971).
[6]K. J. Duff and T. P. Das, Phys. Rev. B **1**, 192 (1968).
[7]D. Tsui, Phys. Rev. **164**, 669 (1967).
[8]R. W. Stark, Phys. Rev. **162**, 589 (1967).
[9]R. W. Stark and L. R. Windmiller, Cryogenics **8**, 272 (1968).
[10]R. W. Stark (unpublished).
[11]F. M. Mueller, Phys. Rev. **148**, 536 (1966).
[12]F. M. Mueller and M. G. Priestly, Phys. Rev. **148**, 538 (1966).
[13]L. Falicov and M. J. G. Lee, Proc. R. Soc. A **304**, 319 (1968).
[14]J. C. Slater and G. F. Koster, Phys. Rev. **94**, 1498 (1954).
[15]J. F. Cornwell, D. M. Hum, and K. C. Wong, Phys. Lett. **26**, 365 (1968).
[16]L. Hodges, D. R. Stone, and A. V. Gold, Phys. Rev. Lett.

19, 655 (1968).
[17]A. V. Gold, J. Appl. Phys. **39,** 768 (1968).
[18]R. W. Stark and L. M. Falicov, in *Progress in Low Temperature Physics*, edited by C. J. Gorter (North-Holland, Amsterdam, 1967), Vol. 5, Chap. 6.
[19]E. Fawcett and W. A. Reed, Phys. Rev. **136,** 422 (1964).
[20]G. W. P. Rengstorf, Battelle Research Report on Preparation and Analysis of High-Purity Iron, Battelle Memorial Institute, Columbus, Ohio, 1966 (unpublished).
[21]Fifty percent saturated ammonium persulfate in water.
[22]R. W. Stark (private communication).
[23]W. C. Black, W. R. Roach, and J. C. Wheatly, Rev. Sci. Instrum. **35,** 587 (1964).
[24]Crystalonics Corp., Newton, Mass.
[25]L. Onsager, Philos. Mag. **43,** 1006 (1952).
[26]R. F. Girvan, A. V. Gold, and R. A. Phillips, J. Phys. Chem. Solids **29,** 1485 (1968).
[27]W. M. Walsh and C. C. Grimes, Phys. Rev. Lett. **13,** 523 (1964).